Ultrasound Molecular Imaging for the Guidance of Ultrasound-Triggered Release of Liposomal Doxorubicin and Its Treatment Monitoring in an Orthotopic Prostatic Tumor Model in Rat

Alexandre Helbert, Mathew von Wronski, Jean-Louis Mestas, Isabelle Tardy, Thierry Bettinger, Cyril Lafon, Jean-Marc Hyvelin, Frédéric Padilla

Ultrasound molecular imaging for the guidance of ultrasound-triggered release of liposomal doxorubicin and its treatment monitoring in an orthotopic prostatic tumor model in rat.

A. Helbert[1] MSc; M. von Wronski[1], PhD; J-L. Mestas[2], PhD; I. Tardy[1], PhD; T. Bettinger[1], PhD; C. Lafon[2], PhD; J-M. Hyvelin[3], PhD and F. Padilla, PhD[2, 4, 5]

From:

[1] Bracco Suisse SA, Bracco Global Research & Development, Plan-Les-Ouates, Geneva, Switzerland. [2] LabTAU, INSERM, Centre Léon Bérard, Université Lyon 1, Univ Lyon, F-69003, LYON, France. [3]Former employee of Bracco Suisse S.A. [4] FUS Foundation, Charlottesville, VA 22903. [5] Dpt of Radiology, University of Virginia School of Medicine, Charlottesville, VA 22903

Author for correspondence:

Alexandre Helbert

Bracco Suisse SA, 31 route de la Galaise, CH-1228 Plan-Les-Ouates, Switzerland.

Phone: +41 22 884 88 17 Fax: +41 22 884 88 85

e-mail: alexandre.helbert@bracco.com

Abstract:

Liposome encapsulation of drugs is an interesting approach in cancer therapy to specifically release the encapsulated drug at the desired treatment site. In addition to thermo-, pH-, light-, -enzyme or redox-responsive liposomes, which have had promising results in (pre-) clinical studies, ultrasound-triggered sonosensitive liposomes represent an exciting alternative to locally trigger the release from these cargos. Localized drug release requires precise tumor visualization to produce a targeted and ultrasound stimulus. We used ultrasound molecular imaging (USMI) with BR55, a vascular endothelial growth factor receptor 2 (VEGFR2)-targeted ultrasound contrast agent, to guide ultrasound-triggered release of sonosensitive liposomes encapsulating doxorubicin (L-DXR) in an orthotopic prostatic rodent tumor model. Forty-eight hours after L-DXR injection, local release of doxorubicin was triggered with a confocal ultrasound device with two focused transducers, 1.1-MHz center frequency, and peak positive and negative pressures of 20.5 and 13 MPa at focus. Tumor size decreased by 20% in 2 wk with L-DXR alone ($n = 9$) and by 70% after treatment with L-DXR and confocal ultrasound ($n = 7$) ($p < 0.01$). The effect of doxorubicin on perfusion/vascularity and VEGFR2 expression was evaluated by USMI and immunohistochemistry of CD31 and VEGFR2 and did not reveal differences in perfusion or VEGFR2 expression in the absence or after the triggered release of liposomes. USMI can provide precise guidance for ultrasound-triggered release of liposomal doxorubicin mediated by a confocal ultrasound device; moreover, the combination of B-mode imaging and USMI can help to follow the response of the tumor to the therapy.

Key words:

Prostate tumor, confocal ultrasound, doxorubicin, sonosensitive liposomes, ultrasound molecular imaging, BR55, treatment monitoring, cavitation.

Introduction

Liposome-encapsulated drugs have been a fast-growing field of research since approval of the PEGylated unilamellar liposome-encapsulated doxorubicin Doxil in 1995 for the treatment of Kaposi's sarcoma (James 1995). Doxil was subsequently approved for metastatic breast cancer, ovarian cancer and multiple myeloma (Goncalves et al. 2020). To date, several formulations of liposome-based products are in clinical trials or approved for different purposes, including analgesics, photodynamic therapy, fungal diseases, viral vaccines and cancer therapy (Bulbake et al. 2017; Goncalves et al. 2020). The advantages of liposomal formulations compared with free drugs include an extended circulation time in blood, reduced side effects (Horowitz et al. 1992; Thorn et al. 2011) and intratumor accumulation through the so-called enhanced permeability and retention effect (EPR) described in the 1980s (Matsumura and Maeda 1986). Despite these advantages, one of the main limitations of liposomal doxorubicin formulations remain the relatively small number of injected liposomes that can reach and finally accumulate within the tumor space (Golombek et al. 2018). This weak accumulation, combined with the slow release of the drug from the liposome, prevents the therapeutic window from being reached and therefore may limit the efficacy.

Although the EPR effect has been largely described in several animal models, its occurrence in patients remains debated (Moghimi and Farhangrazi 2014; Nichols and Bae 2014; Golombek et al. 2018; Swetha and Roy 2018; Zhou et al. 2020), and several strategies to improve the EPR effect have been investigated as a way to increase the concentration of liposomes at the target site, including alteration of the tumor micro-environment and endothelial cell lining, aided by external sources such as radiation, hyperthermia, photodynamic therapy and ultrasound (Dhaliwal and Zheng 2019; Park et al. 2019).

Another approach to potentiate liposomal drug-based treatment is to locally trigger the release of the drug from the liposome to increase its bioavailability in a short period and reach a therapeutic window. With respect to the latter approach, formulations of thermo-, pH-, light-, enzyme- or redox-responsive liposomes have shown promising results in preclinical and clinical studies (Lee and Thompson 2017; Abri Aghdam et al. 2019). In a phase 1 clinical trial using ultrasound-induced hyperthermia to trigger targeted drug delivery of doxorubicin from thermosensitive liposomes (TARDOX study), the use of ultrasound-induced hyperthermia resulted in an enhanced delivery of doxorubicin in solid liver tumors (Lyon et al. 2018; Gray et al. 2019). Formulations of liposomes that can release their cargo in response to the mechanical ultrasound stimulus of cavitation, so-called sonosensitive liposomes, have also been investigated. In this context, Evjen et al. (2011) have described a sonosensitive liposomal doxorubicin (L-DXR) formulation based on the unsaturated phospholipid 1,2-dierucoyl-sn-glycero-3-phosphocholine.

By use of a dedicated confocal ultrasound device to induce mechanical stress on the liposomes through acoustic cavitation, precise release of encapsulated drug could be triggered on demand (Somaglino et al. 2011; Evjen et al. 2013). Previous studies have found in vitro that the degree of release from these liposomes is proportional to the cavitation dose applied, and that under cavitational stress, more than twice the amount of DXR is released compared with the clinical formulation Caelyx (Mestas et al. 2014). This cavitational procedure was successfully tested in vivo in a subcutaneous rat prostatic carcinoma model (AT2 phenotype of the Dunning R3327) in which the activation of L-DXR 48 h postinjection limited tumor growth (Fowler et al. 2013; Mestas et al. 2014). Such inertial cavitation treatment does not alter the structure and cytotoxicity of doxorubicin, is safe and did not promote cancer cell dissemination in a highly metastatic 4T1 breast tumor model in mice (Lafond et al. 2016).

Moreover, pulsed cavitational ultrasound was successfully tested to treat calcified bioprosthetic valve stenosis (Villemain et al. 2017) and a First-in-Man clinical trial has been conducted to remotely treat aortic stenosis (NCT03779620).

An important constraint to locally trigger the release of doxorubicin from liposomes is the need for treatment guidance on precise application of the cavitation stimulus. This need was highlighted when tested in an orthotopic pancreatic murine model (Camus et al. 2019), in which the use of a very high frequency (40 MHz) preclinical ultrasound scanner was required to localize the tumor and guide the treatment.

For the clinical treatment of tumors in deep organs such as the prostate and pancreas, where such high-frequency imaging is not possible, the use of gas microbubbles as intravascular ultrasound contrast agents is an alternative imaging option (Wang et al. 2020; Klibanov 2021). Thus, contrast-enhanced ultrasound (CEUS) would be an asset as it offers real-time imaging with high spatial resolution to delineate the lesion's extent and can also provide valuable information on perfusion (Frinking et al. 2020). Although 3-D matrices are available, and the feasibility of 3-D CEUS imaging in humans has been reported (Xiang et al. 2013; Sridharan et al. 2015; El Kaffas et al. 2017), as has its ability to identify responders to different cancer therapies based on monitoring of perfusion changes (El Kaffas et al. 2020), 3-D CEUS imaging is currently the standard in clinics, which limits its attractivity for treatment guidance.

Ultrasound molecular imaging (USMI) could provide an even more specific alternative, as tumor visualization and delineation based on the detection of specific tumor endothelial characteristics could be achieved (Wang et al. 2020). USMI has been validated in preclinical models using cationic microbubbles (Diakova et al. 2020), targeted microbubbles against von Willebrand factor (Shim et al. 2015), αv-integrins (Leong-Poi et al. 2003) or tumoral biomarkers, including B7 H3 (Bachawal et al. 2020), Netrin 1 (Wischhusen et al. 2018) and

vascular endothelial growth factor receptor 2 (VEGFR2) with BR55 (Pochon et al. 2010). BR55 was tested in an orthotopic prostatic G-Dunning model, where the feasibility of tumor visualization in the prostate was determined (Tardy et al. 2010). In a chemo-induced rat mammary tumor model, it was found that USMI can provide a volumetric tumoral delineation and that the therapeutic follow-up of tumoral response to an anti-angiogenic treatment is feasible at the anatomical, functional and molecular levels in a single exam (Helbert et al. 2020). Recently, BR55 has been successfully translated in the clinic for the detection of angiogenesis in breast and ovarian tumors in women (Willmann et al. 2017) and prostate cancer in men (Smeenge et al. 2017).

In the present study, we used USMI with BR55 to guide ultrasound-triggered release of liposomal doxorubicin in a preclinical prostate tumor model. Sonosensitive L-DXR were injected into rats bearing orthotopic G-Dunning rat prostate tumors. USMI was used to visualize and delineate tumors within the prostate to specifically select ultrasound treatment locations. Finally, USMI was used to evaluate tumor response after ultrasound-induced doxorubicin release from liposomes.

Material and methods

Orthotopic prostate tumor animal model.

All animal procedures were approved by the Cantonal Veterinary Office of Geneva. Orthotopic prostatic adenocarcinomas were induced by injection of 2 × 106 G-Dunning R3327 cells (ECACC, Salisbury, UK) into the right ventral lobe of the prostate of Copenhagen rats (Charles River Laboratories, Les Oncins, France; 220–250 g) according to Tardy et al. (2010). From 6 wk after injection and then at least once a week, B-mode imaging was performed to visualize tumor appearance and growth. Animals were enrolled in the study when their tumors reached ∼0.2 cm^2 in their largest cross-section.

Sonosensitive liposomal doxorubicin.

[1,2-Dierucoyl-sn-glycero-3-phosphocholine]-based liposomal doxorubicin (L-DXR) was prepared according to Afadzi et al. (2013) with an improvement for doxorubicin loading and free doxorubicin disposal. Liposomes are composed of DEPC : 1,2-Dierucoyl-sn-glycero-3-phosphocholine (DEPC, Nof Corp., Tokyo, Japan); DSPC : 1,2-distearoyl-sn-glycero-3-phosphocholine (DSPC, Genzyme, Cambridge, MA, USA); 1,2-distearoyl-sn-glycero-3-phosphorylethanolamine–polyethylene glycol 2000 (DSPE–PEG2000, Genzyme); and cholesterol (Merck, Darmstadt, Hesse, Germany) (52:5:8:35) with a lipid:doxorubicin ratio of 16:1. Doxorubicin (Ref. No. D-4000, LC Laboratories, Woburn, MA, USA) solution was added to the liposome solutions and placed in a water bath (48°C, 1 h). After being cooled to room temperature, free doxorubicin was discarded by tangential flow filtration dialysis using the tangential flow filtration system (Pelikon membrane, cutoff 100,000, Millipore, Burlington, MA, USA) against a solution of 255 mM sucrose (Sigma-Aldrich Chemie GmbH, Buchs, Switzerland) and 10 mM Hepes buffer (Sigma-Aldrich), pH 7.4. Finally, size distribution was

157 determined using the Zetasizer 3000 HSA (Malvern Panalytical Ltd, Malvern, UK). L-DXR was
158 injected via the tail vein at the dose of 3 mg of doxorubicin/kg in the different experiments.
159
160 *Study design.*
161 The pharmacokinetics of L-DXR was evaluated in nine animals; the doxorubicin in
162 blood, prostate and tumor was measured at 24 h (n = 2), 48 h (n = 3) and 72 h (n = 4). For
163 comparison, doxorubicin in its free form (F-DXR) was injected into seven animals and
164 measured at 24 h (n = 2), 48 h (n = 3) and 72 h (n = 2) (Fig. 1a). Potential histopathological
165 effects resulting from an acute confocal US treatment of the tumor and its surrounding tissues
166 were verified first in five animals (n = 5). For that, animals were euthanized after a 20-min
167 period, and tissues were sampled for histopathological evaluation. In the second step, the
168 effect of $US_{confocal}$ alone on tumor growth was monitored with B-mode over a 7-d period in
169 five animals (n = 5) and compared with the effects on naïve untreated tumor (n = 4), L-DXR-
170 treated tumor (n = 9) and L-DXR + $US_{confocal}$ -treated tumors (n = 7) (Fig. 1b).
171 In a third step, a follow-up at 14 d was performed specifically on two groups—L-DXR
172 (n = 9 at days 0, 4 and 7; n = 6 at days 9 and 14) and L-DXR + $US_{confocal}$ (n = 7 at days 0, 4 and 7;
173 n = 5 at days 9 and 14)—to evaluate the efficacy of the cavitational treatment in potentiating
174 the effect of liposomal doxorubicin. As seen on the timeline (Fig. 1c), tumor area was
175 measured at days 0, 4, 7, 9 and 14 in B-mode; USMI was performed at days 0, 7 and 14 to
176 measure peak enhancement and signal of bound BR55 microbubbles. During the long-term
177 follow-up, tumors from the L-DXR and L-DXR + $US_{confocal}$ groups were harvested for
178 immunohistochemistry (IHC) at day 7 (n = 3 and n = 2, respectively) and day 14 (n = 6 and n =
179 5, respectively) and compared with untreated tumors (n = 6).
180

Pharmacokinetics of Sonosensitive liposomal doxorubicin.

Free doxorubicin and L-DXR were intravenously injected at the dose of 3 mg of doxorubicin/kg, and rats were euthanized after 24, 48 or 72 h. Blood was sampled from the abdominal aorta into heparin tubes under deep gaseous anesthesia. Then, blood samples were centrifuged 10 min at 10,000 g to obtain plasma. Tumor and healthy prostate samples were also collected and stored in –80°C isopentane. Doxorubicin content in both plasma and tissue samples was determined using high-performance liquid chromatography (HPLC) coupled with a fluorescence detection (Agilent, Santa Clara, CA, USA). For HPLC analyses, a Luna reverse-phase C18 column (Phenomenex, Basel, Switzerland) was used, and fluorescence detection was performed with excitation and emission wavelengths set at 475 and 550 nm, respectively.

Tumor growth follow up and USMI of VEGFR2.

Anesthesia was achieved with isoflurane (Attane, Provet AG, Lyssach, Switzerland) inhalation in an induction box (5% isoflurane v/v in 1 L/min air) and maintained at 2% (v/v) isoflurane 0.8 L/min during the experiment. Skin at the abdominal level above the prostate was prepared by removing hair using a depilatory cream (Veet, Reckitt Benckiser, Slough, UK). Then, an ultrasonic coupling gel (Aquasonic 100, Parker, Fairfield, NJ, USA) was applied between the ultrasound probe and the skin.

For tumor growth (B-mode) and USMI (contrast mode), side-by-side acquisitions were performed using the L12-5 transducer (central frequency = 5 MHz, spatial resolution = 0.14 mm) operating with an iU22 diagnostic ultrasound scanner (Philips, Bothell, WA, USA).

Delimitation of tumors was performed in B-mode for tumor growth follow-up as previously described (Helbert et al. 2020) and automatically pasted on contrast images. USMI

of VEGFR2 was performed before the injection of L-DXR and then after 7 and 14 d. Intermittent (1 Hz) power modulation imaging mode at a non-destructive mechanical index (MI = 0.08), contrast general (CGen) mode, compression of 38, time compensation gain linear and focus at the level of the organ (Xres) was used to monitor the signal corresponding to the arrival of BR55 during the wash-in phase and the accumulation of BR55 in the tumor 10 min after injection.

USMI was performed using BR55 injected as a single bolus of 3 × 108 microbubbles/kg. Microbubbles were injected using a semi-automated system as previously described by Hyvelin et al. (2013). At each USMI session, the transducer was positioned to visualize the largest cross-section of the tumor, and BR55 arrival was attained during the first 40 s. Then, insonation was stopped for 10 min to allow clearance of circulating microbubbles. Insonation was finally resumed for 10 s to acquire late-phase enhanced signal arising from bound microbubbles. Signal from residual circulating microbubbles was then acquired after a flash destruction sequence at high mechanical index (MI = 1.9). Ultrasound imaging sequences were exported in DICOM format for offline analysis using VueBox quantification software (Bracco Suisse S.A., Plan-les-Ouates, Switzerland). Peak enhancement (PE) was extracted from time–intensity curves according to Tranquart et al. (2012). Signal from bound microbubbles (differential tissue enhancement [dTE]) was assessed 10 min after injection of BR55 according to the method introduced by Desphande et al. (2010).

Confocal ultrasound treatment.

Confocal ultrasound treatment was performed 48 h after injection of doxorubicin liposomes, $US_{confocal}$ was delivered to anesthetized animals placed in a custom-made rubber bed with a treatment window at the level of the prostate (Fig. 2a). The confocal ultrasound

device is composed of two focused single-element transducers (focal length = 50 mm, radius of curvature = 50 mm, central frequency = 1.1 MHz) tilted at a 110° angle, with a central linear transducer (L12-5) in between (Mestas et al. 2014). The linear probe was used to visualize the binding of BR55 in the tumor and, therefore, to delineate a conformational treatment area (Fig. 2b). Three-dimensional USMI, to delineate the tumor, was performed by scanning the tumor—from one pole to the other pole. Then, BR55 microbubbles were destroyed before $US_{confocal}$ treatment over the entire tumor by increasing the mechanical index. The confocal ultrasound device was placed below the bed in a degassed water tank at a temperature of 37°C. $US_{confocal}$ treatment of the entire tumor was achieved by 3-D displacement of the bed (using an ESP300 motor controller, Newport, Irvine, CA, USA). Tumors were treated in planes separated by 2 mm. Within each plane, treatment points were separated by 2 mm. This 2-mm spacing was chosen relative to the size of the cavitation cloud (Fig. 2c) and to ensure uniform treatment of all treatment planes (Mestas et al. 2014). US insonation (pulse repetition frequency = 250 Hz, burst count = 44 cycles, duty cycle (DC) = 1%, pulse duration = 2 s) was applied from one pole to the other (Fig. 2c). The confocal ultrasound device delivers, at the focus, peak positive and negative pressures of 20.5 and 13 MPa, respectively (Mestas et al. 2014), optimized to generate cavitation in situ (Lafond et al. 2016; Camus et al. 2019).

Immunohistochemistry and grading of CD31/VEGFR2 expression.

On completion of the study, bladder, seminal vesicles and prostate were harvested en bloc and stored in 2-methylbutane (Sigma-Aldrich Chemie GmbH) at –80°C. Immunofluorescence staining of both VEGFR2 and CD31 of the largest cross section on 10-µm-thick slices was achieved as follows. VEGFR2 and CD31 were stained with rabbit anti-human VEGFR2 (0.26 µg/mL, Ref. No. 2479, monoclonal antibody, Cell Signaling Technology,

Danver, MA, USA) and mouse anti-rat CD31 (1 µg/mL, Ref. No. MCA1334G, monoclonal antibody, AbDSerotec, Hercules, CA, USA). Primary antibody was then revealed with a fluorescent secondary antibody, Alexa 488 goat anti-rabbit serum (Ref. No. A31570, Invitrogen, Waltham, MA, USA) or Alexa 555 donkey anti-mouse serum (Ref. No. A11008, Invitrogen), both used at 2 µg/mL. For blood vessels (CD31) and VEGFR2 (KDR) immunofluorescence grading, five fields of view (FOV) were randomly chosen, and three blinded readers performed grading. A score between 0 and 3 (steps of 0.5) was given, and for each FOV, the mean score of the three blinded readers was calculated.

Histopathological assessment of tissue after $US_{confocal}$ insonation

Animals were sacrificed 20 min after $US_{confocal}$ treatment alone. For this evaluation, $US_{confocal}$ was performed on the whole prostate, including the tumor and seminal vesicles. Tissues were then fixed in formol. Sections (4 µm thick) were stained with hematoxylin and eosin for further histopathological evaluation by a skilled pathologist.

Confocal scanning laser scanning microscopy of intratumoral doxorubicin distribution.

Two days after $US_{confocal}$ treatment, 100 µg of tomato lectin fluorescein (Ref. No. FL-1171, Vector Laboratories, Burlingame, CA, USA) was injected via the tail vein 5 min before sacrifice. Tumors (n = 2) were harvested and fixed in –80°C isopentane before cryosectioning. Cryosections 30 µm thick were obtained and Microscope slide in Vectashield antifade mounting medium (Vector Laboratories, Ref. No. H-1000). Tumor samples were imaged with a confocal microscope (Zeiss 780, objectives Plan-Apochromatic 10 × /0.45 M27 and Plan-Apochromatic 63 × /1.40 Oil DIC M27, Zeiss, Oberkochen, Deutschland), for doxorubicin at 488/591 nm and for lectin at 488/515 nm (excitation/emission).

Statistical analysis

Data are reported as the mean ± standard deviation (SD). For evaluation of tumor growth rate, tumor area at day 7 was normalized to that at day 0; and a two-way analysis of variance (ANOVA) with post hoc Bonferroni analysis was performed to evaluate the effect of time and treatment. One-way ANOVA with post hoc Bonferroni analysis was used to compare tumor size over time in L-DXR and L-DXR plus US groups. An unpaired t-test was used for matched days comparison between L-DXR and L-DXR plus US groups. A p value <0.05 was considered to indicate significance. Statistical analyses were performed using GraphPad Prism Version 5.01 Software (GraphPad Software, San Diego, CA, USA).

Results

Home-made liposome pharmacokinetic and biodistribution in plasma and organs.

Doxorubicin liposomes (L-DXR) had a mean diameter of 91 nm, and the concentration of doxorubicin was 1.1 mg/mL.

In plasma, doxorubicin cleared more rapidly in its free form (F-DXR) than in the liposomal formulation (L-DXR). Twenty-four hours after injection of F-DXR, doxorubicin within the plasma represented ~0.5% of the initial dose (n = 2). Conversely, in rats injected with L-DXR, plasma doxorubicin represented 46.7%, 17.9% and 8.1% of the initial dose, respectively, at 24 h (n = 2), 48 h (n = 3) and 72 h (n = 4) post-injection (Fig. 3a). In all animals, doxorubicin levels remained low in healthy prostate and tumor when injected as F-DXR, with the amount of accumulated doxorubicin representing less than 0.06% of the injected dose at 48 h. Conversely, when L-DXR was injected, peak accumulation of doxorubicin in tumors was reached 48 h post-injection, with a 16-fold increase compared with the healthy prostate ($p < 0.05$) and 5-fold and 9-fold increases at 24 and 72 h, respectively (Fig. 3b). For the remainder of the study, confocal ultrasound treatment was applied 48 h after L-DXR injection to treat at the peak doxorubicin accumulation in the tumors.

Histopathological assessment of tissue after $US_{confocal}$ treatment.

In rats (n = 5) treated with $US_{confocal}$ alone, histopathological evaluation revealed no signs of abnormalities, as indicated by the absence of edema, hemorrhage, necrosis or inflammatory cells within the tumor (Fig. 4). It is noteworthy that in this group, the tumor, as well as the bladder, healthy prostate and seminal vesicle and urinary tract, were insonified. None of these organs exhibited signs of abnormalities.

311

312 *Tumor growth over a 7-d period.*

313 Tumor growth was first observed over a 7-d period before tumors in the untreated
314 animals reached ethical limits. There were no significant differences among the four
315 experimental conditions: no treatment, $US_{confocal}$, L-DXR and L-DXR + $US_{confocal}$ ($p = 0.52$). At
316 day 7, tumor size measurements revealed significant differences between treatment
317 conditions, $p < 0.05$. A 2.2-fold increase in size was measured in the untreated group (+ 120%)
318 and a 1.5-fold increase was measured in the $US_{confocal}$ group (+ 50%), suggesting a slight
319 response to $US_{confocal}$ treatment. In the L-DXR group, tumor size remained unchanged (+ 4.9%).
320 Finally, a stronger and significant effect ($p < 0.001$ compared with L-DXR, $US_{confocal}$ and
321 untreated groups) was observed when the $US_{confocal}$ treatment occurred 48 h after injection of
322 L-DXR, with a 3-fold decrease in size (–66%) (Fig. 5).

323

324 $US_{confocal}$ *treatment potentializes the effect of doxorubicin.*

325 In animals treated with L-DXR, the impact of $US_{confocal}$ treatment on tumor growth was
326 evaluated 4, 7, 9 and 14 d after injection, while tumor size remained below ethical limits (Fig.
327 6). In the absence of $US_{confocal}$ treatment, tumor area slightly increased (non-significantly)
328 between days 0 and 4 (0.29 ± 0.07 cm² [n = 9] at day 4 vs. 0.25 ± 0.04 cm² [n = 9] at day 0) and
329 then gradually decreased up to day 14 to 80% of the initial size (0.20 ± 0.05 [n = 6]). When
330 $US_{confocal}$ treatment occurred 48 h after injection of L-DXR, a faster and more pronounced
331 decrease was observed. Indeed, a 1.5-fold reduction (–68%) was observed at day 4 (0.19 ±
332 0.12 cm² [n = 7] vs. 0.28 ± 0.07 cm² [n = 7] at day 0). Then, tumor shrinkage occurred up to day
333 9 (0.08 ± 0.03 cm² [n = 4]) and remained stable until the end of treatment; (0.08 ± 0.02 cm² [n
334 = 5]). Comparison of tumor size between L-DXR and L-DXR + $US_{confocal}$ daily revealed a

335 statistically significant difference between the two experimental conditions starting at day 7
336 ($p < 0.05$).
337
338 *Perfusion and VEGFR2 expression assessed by USMI with BR55*
339 To assess the ability of USMI to follow alteration in perfusion and expression of VEGFR2
340 after therapy, changes in peak enhancement (PE) and signal from bound BR55 microbubbles
341 (differential tissue enhancement [dTE]) were evaluated. At baseline, PE, a marker of perfusion,
342 was similar during arrival of BR55 in the L-DXR (19,060 ± 6825 a.u. [n = 9]) and L-DXR + $US_{confocal}$
343 (12,951 ± 8121 a.u. [n = 7]) groups, p = 0.12. $US_{confocal}$ treatment had no impact on PE, as no
344 significant difference was observed between the L-DXR and L-DXR + $US_{confocal}$ groups at days 7
345 and 14 (27,883 ± 11,210 a.u. [n = 9] vs. 12,591 ± 8121 a.u. [n = 7, p = 0.46] and 32,592 ± 9283
346 a.u. [n = 6] vs. 21,131 ± 7449 a.u. [n = 5, p = 0.05], respectively) (Fig. 7a).
347 Molecular assessment with USMI, which reflects the levels of VEGFR2 expression in tumor
348 vessels, presented a similar dTE in the L-DXR and L-DXR + $US_{confocal}$ groups at day 0 (890 ± 221
349 a.u. [n = 9] vs. 697 ± 411 a.u. [n = 7], respectively, p = 0.21). In agreement with
350 immunohistochemistry, no significant differences were observed in response to treatments
351 at days 7 and 14 (1130 ± 693 a.u. [n = 9] vs. 825 ± 353 a.u. [n = 7], p = 0.4227, and 705 ± 288
352 a.u. [n = 6] vs. 674 ± 338 a.u. [n = 5], p = 0.90, respectively, in the L-DXR and L-DXR + $US_{confocal}$
353 groups) (Fig. 7b).
354
355 *Assessment of CD31 and VEGFR2 expression by immunohistochemistry.*
356 To further assess the effect of the cytotoxic therapy triggered by DXR administration
357 on CD31 and VEGFR2 expression, we performed immunostaining in a subset of prostatic
358 tumors harvested 7 and 14 d after the injection of L-DXR, as well as in a subset group of tumors

359 from untreated rats. In L-DXR and L-DXR + $US_{confocal}$ groups, semiquantitative grading of CD31
360 revealed similar and sustained expression at both days 7 and 14. Semiquantitative assessment
361 of VEGFR2 expression also revealed sustained expression in the L-DXR + $US_{confocal}$ group. A
362 slight decrease was observed in the L-DXR group at day 14 (1.8 ± 0.07 a.u., n = 6) compared
363 with untreated animals (2.3 ± 0.5 a.u., n = 6, p = 0.07) and L-DXR + $US_{confocal}$ -treated animals
364 (2.3 ± 0.4 a.u., n = 5, P = 0.11), but was non-significant (Fig. 8).
365
366 *Confocal scanning laser scanning microscopy of intratumoral doxorubicin distribution.*
367 In the preliminary confocal microscopy observations (n = 2), doxorubicin was found to
368 be located mainly in the perivascular space in our model, and L-DOX was internalized by tumor
369 cells localized mainly at the tumor's edge (Fig. 9).
370

Discussion

A therapeutic benefit of a combination of confocal ultrasound with sonosensitive liposome-encapsulated doxorubicin was determined in this study in an orthotopic model of prostatic adenocarcinoma in rats. USMI using BR55 was first used to delineate tumor within the prostate, prior to the insonation of sonosensitive liposomes with a dedicated confocal ultrasound device. B-Mode imaging and USMI were then used to monitor tumor response to the cytotoxic therapy at the anatomical, functional and molecular levels in a single procedure, a method previously validated in a rat mammary tumor model treated with an anti-angiogenic drug (Helbert et al. 2020).

The ultrasound treatment, applied using confocal ultrasound to induce cavitation and mechanical ultrasound-tissue interactions, has been proven to be safe in preclinical tumor models (Lafond et al. 2016). It was applied in our study with the intent of triggering the release of doxorubicin from the encapsulating liposomes. In an in vitro setting, it was recently reported that this type of pulsed ultrasound can also potentiate the toxicity of doxorubicin (Fant et al. 2019). Numerous other bio-effects associated with ultrasound-induced cavitation have been reported when nucleation agents such as ultrasound contrast agents were used to trigger cavitation activity, in the field of sonoporation, or transient permeabilization of plasma membrane (Escoffre et al. 2013), augmentation of nuclear pores (Furusawa et al. 2014) or induction of single- and double strand breaks (Kondo and Yoshii 1985). Some effects may have contributed to the potentiation of DXR observed in our study, in which cavitation was generated in situ without the use of ultrasound contrast agents, as previously reported (Lafond et al. 2016; Camus et al. 2019). Additionally, pulsed ultrasound treatments have been reported to be able to induce or modulate an anti-tumor immune response, through

suppression of anti-inflammatory cytokines (Aydin et al. 2019), which may be at play in our experiments.

The cytotoxic drug doxorubicin was administered by means of homemade sonosensitive liposomal doxorubicin (L-DXR). As expected, the circulation time of L-DXR was dramatically extended compared with that of free doxorubicin in blood, with almost 20% of the injected dose still in circulation after 2 d. If this longer circulation time and the leaky vasculature of angiogenic tumors are taken advantage of, L-DXR could specifically accumulate in tumor through the EPR effect, whereas the level of doxorubicin would remain low in healthy prostate tissues. Indeed, our results indicate a 9-fold increase in doxorubicin in the tumor, compared with healthy prostate, 48 h after injection of L-DXR. Although the amount of doxorubicin detected in the tumors remained a small fraction of the injected dose (~0.5%), it has been reported that a dose as little as 0.7% of the initial dose could be enough to induce a therapeutic effect (Golombek et al. 2018). On the basis of our finding and in line with the procedure previously used by others (Mestas et al. 2014; Camus et al. 2019), local release of the doxorubicin from L-DXR in the tumor was induced 48 h post-injection using the dedicated confocal ultrasound device. Treatment planning was made easier using USMI with BR55 to delineate the tumor, particularly because B-mode imaging was suboptimal in our setup because of the long distance between the imaging probe and the tumor when the animals were positioned in the water tank. We also hypothesized that this approach would be helpful when lesions and tumor boundaries are difficult to visualize within an organ, as is the case for prostate cancer on B-mode ultrasound. Furthermore, BR55 was used to monitor tumor response and treatment efficacy over a 2-wk period through the assessment of VEGFR2 accessibility to the microbubbles that is linked to the expression of this receptor, as well as

through a functional characterization of the tumor perfusion that is related to the density of microvessels.

$US_{confocal}$ treatment alone had a limited effect on tumor growth control after 7 days in comparison to untreated tumors. In the same time interval, L-DXR alone was able to contain tumor growth. More interestingly, the combination of L-DXR and confocal ultrasound had a marked effect on tumor growth, with a ∼70% reduction in tumor size after 14 d. The added value of confocal ultrasound was evidenced starting 4 d after injection of L-DXR, 2 d after insonation, with a significant decrease in tumor size, while in the meantime tumor size increased in the L-DXR group. Together, these results illustrate that confocal ultrasound potentiated liposomal doxorubicin, resulting in increased therapeutic efficacy.

Peak enhancement in the largest tumor cross-section over time compared with day 0 did not statistically significantly differ between the L-DXR and L-DXR + US groups. These results were confirmed by immunochemistry of CD31, which also revealed a stagnation of vascular density. Finally, the signal of BR55-bound microbubbles was not modified 7 and 14 d after the injection of L-DXR, without or with insonation. The latter results are supported by immunohistochemistry indicating a stable expression of VEGFR2 over the 2 wk.

Analyses of both BR55-bound microbubbles and the immunohistochemistry data revealed that treatment with L-DXR, with or without focused ultrasound, did not affect VEGFR2 expression over the 2-wk follow-up, suggesting that VEGFR2 expression was not modified. A tumor size reduction associated with stable VEGFR2 expression is not in itself surprising. A reduction of tumor size together with a stable signal for bound BR55 microbubbles has been reported in a study of tumors treated with imatinib, an anti-angiogenic specific to platelet-derived growth factor receptor (PDGFR), whereas in tumors treated with sunitinib, which acts directly on VEGFR2, a decrease in tumor size was associated with a

441 decrease in BR55 signal (Payen et al. 2015). In another preclinical study using homemade
442 VEGFR2 microbubbles and a new imaging technology called targeted molecular localization
443 (TML), Zhao et al. (2021) also observed a decrease in signal from microbubbles in sunitinib-
444 treated tumors. We therefore hypothesized that in our experiment, endothelial cells were not
445 the main target of the treatment. An indirect anti-angiogenic effect of L-DXR has been
446 reported in another tumor model (MDA-MB-231), but only because the high- density
447 extracellular matrix limited the diffusion of L-DXR into the perivascular space and the
448 doxorubicin was released close to the endothelial cells (Kibria et al. 2016). The density of the
449 extracellular matrix was not evaluated in the G-Dunning prostate tumor model used here, but
450 preliminary confocal microscopy observations suggest that doxorubicin could reach the
451 perivascular space in our model and that L-DXR was internalized by tumor cells localized
452 mainly at the tumor's edge. These observations suggest that the action of the cytotoxic drug
453 was peripheral, maintaining a tumoral core with vascularity and VEGFR2 unaffected. We
454 therefore assume that peripheral prostatic tumor cells were the main target of liposomal
455 doxorubicin leading to decreased tumor volume but sustained PE and BR55-bound signal
456 expression within the residual tumor. Repeated treatments may be required to affect the
457 entirety of the tumor.

458 Our study has limitations. First, rats treated with US alone were followed only 7 d post-
459 treatment, thereby limiting the long-term analysis of the effect of focused US on tumor
460 growth. A longer evaluation period would make it possible to determine whether the
461 observed effect would continue or, on the contrary, the tumor relapsed. Further, confocal
462 microscopy evaluation was performed on only two tumors, and imaging of a larger number of
463 specimens would be required to draw definitive conclusions. Finally, imaging of CD31 does
464 not necessarily inform on the functionality of the vessels, and a combination of CD31 and

lectin as used for confocal microscopy imaging could uncover additional information on the effects of the treatments on the vasculature.

In this study, we determined that sonosensitive liposomes loaded with doxorubicin (L-DXR), when combined with confocal ultrasound treatment, induce a strong reduction in growth of the orthotopic G-Dunning tumor in comparison to L-DXR alone. We highlighted that the use of USMI can be advantageous in delineating tumor boundaries and in helping to guide focused ultrasound treatment. Finally, the use of USMI with BR55 was relevant in following tumor response to this cytotoxic therapy, by delineating residual tumoral tissue. That imaging could potentially be used to further discriminate viable tumor tissue, which could be foci of relapse, from necrosis or fibrotic tissue.

The therapeutic procedure used in this study is based on delivery of cavitational ultrasound with a confocal ultrasound device combined with liposomes for on-demand release and USMI. As the use of therapeutic ultrasound, USMI and nanomedicine are in full expansion and have been separately used in different phases of clinical trials, their combined use could be investigated to offer a global approach to cancer management, that is, diagnosis, treatment and follow-up of solid tumors. Thus, USMI as an imaging modality for treatment planning in US-guided local ablation techniques may become clinically relevant when B-mode is suboptimal. In addition, the use of cavitational ultrasound to improve the effectiveness of L-DXR could lead to improvement in outcomes and/or allow a reduction in the dose of doxorubicin.

Conclusion.

USMI can provide precise guidance for ultrasound-triggered release of liposomal doxorubicin mediated by a confocal ultrasound device. The combination of L-DXR with cavitational ultrasound treatment increases the efficacy of doxorubicin, resulting in a significant reduction in tumor size compared with that obtained with L-DXR treatment alone.

No substantial variations were observed with USMI in perfusion and BR55 signal following liposomal doxorubicin therapy; and this was confirmed by immunohistochemistry, which revealed no change in CD31 and VEGFR2 expression. USMI allows accurate delineation of the residual viable tumor edge and can provide information additional to that obtained with B-mode imaging for treatment planning and follow-up with such combination therapy. In the case of liposomal doxorubicin therapy, where the main target of the drug is tumor cells, BR55 can provide supplemental information to identify areas of the tumors that remain viable.

Acknowledgments

Phillipe Bussat is acknowledged for the preparation of the sonosensitive liposome suspensions. We also thank Florence Séchaud and Samir Cherkaoui for the dosage of doxorubicin.

This work was supported by the LabEx DEVweCAN (ANR-10-LABX-0061) of the University of Lyon, within the program Investissements d'Avenir (ANR-11-IDEX-0007) operated by the French National Research Agency (ANR).

Conflicts of interest disclosure.

A. Helbert, M. von Wronski, T. Bettinger, I. Tardy, J.-M. Hyvelin, were employees of Bracco Suisse SA at the time the study was carried out. F. Padilla, J-L. Mestas and C. Lafon declares no commercial or financial conflict of interest.

Figure legends

Fig. 1 Overview of the protocol design and main steps of the study. (a) Pharmacokinetics and biodistribution of free doxorubicin (F-DXR) and liposomal doxorubicin (L-DOX) in blood, tumor and surrounding tissue. (b) Evaluation of confocal ultrasound ($US_{confocal}$) on histopathology and L-DXR ± $US_{confocal}$ treatments on G-Dunning tumor growth assessed in B-mode over 7 d. (c) Evaluation of L-DXR versus L-DXR + $US_{confocal}$ on G-Dunning tumors with ultrasound molecular imaging (USMI)/B-mode and immunohistochemistry (IHC).

Fig. 2 Confocal ultrasound ($US_{confocal}$) experimental setup. (a) Schematic of the setup. The $US_{confocal}$ device and L12-5 transducer were placed in a 37°C degassed water tank. Above the $US_{confocal}$ device, animals were placed in a bed with a treatment window at the level of the prostate. (b) Side-by-side B-mode and contrast images revealing the signal of BR55-fixed microbubbles in the tumor 10 min after injection. Volumetric delineation of the tumor from one to the other pole was obtained with USMI by scanning the entire tumor volume in 2-mm steps of displacement using the 3-D motion stage (orange lines indicate tumor edges, red lines and green lines indicate the prostate and bladder, respectively). (c) Activation of liposomal doxorubicin (L-DXR) was achieved by US pulses applied every 2 mm over the area previously identified after ultrasound molecular imaging (USMI) of vascular endothelial growth factor receptor 2 (VEGFR2). $US_{confocal}$ pulses could also induce cavitation spots in the tumor (white arrow).

Fig. 3 (a) Pharmacokinetic profiles of free doxorubicin (F-DXR) and liposomal doxorubicin (L-DXR) in plasma 24, 48 and 72 h postinjection expressed as a percentage of the initial dose. (b) Accumulation of F-DXR and L-DXR in healthy prostate and tumor 24, 48 and 72 h postinjection.

Fig. 4 Hematoxylin and eosin staining of tumor and surrounding tissue reveal that confocal ultrasound ($US_{confocal}$) treatment alone does not have acute side effects. Sections were from an untreated rat (top left panel) and rats treated with $US_{confocal}$ (remaining panels). Thin arrows indicate the G-Dunning tumor, thick arrows indicate the bladder, and dashed-line arrows indicate the prostate. The asterisk indicates hyperemia in the blood vessel caused by incomplete exsanguination. Bar = 1 mm.

Fig. 5 Variation in tumor size over a 7-d period in the untreated, confocal ultrasound ($US_{confocal}$) alone, liposomal doxorubicin (L-DXR) alone and L-DXR + $US_{confocal}$ groups. Symbols represent statistical differences between groups (one-way analysis of variance with post hoc Bonferroni analysis: *$p < 0.05$ and ***$p < 0.001$).

Fig. 6 Comparison of tumor growth in size over time in the liposomal doxorubicin (L-DXR) alone (top) and L-DXR + confocal ultrasound ($US_{confocal}$) (bottom) groups. Symbols represent statistical differences between groups at a specific time point (unpaired t-test, *$p < 0.05$, **$p < 0.01$ and ***$p < 0.001$). B-Mode illustrative images at days 0, 7 and 14 are presented for the two groups (white lines indicate the prostate, and white dashed lines, the tumor).

Fig. 7 Comparison of tumor peak enhancement (a) and signal of bound BR55 microbubbles (b) over time in the liposomal doxorubicin (L-DXR) and L-DXR + confocal ultrasound ($US_{confocal}$)

groups. Bottom and top: B-Mode illustrative images at days 0, 7 and 14 for the two groups (tumors are delineated by white lines, delimitation was first done on the B-mode image and automatically pasted on the contrast image). dTE = differential tissue enhancement.

Fig. 8 Left: Semiquantitative grading of CD31 (a) and vascular endothelial growth factor receptor 2 (VEGFR2) (b) expression in prostatic tumors treated with liposomal doxorubicin (L-DXR) and L-DXR + confocal ultrasound ($US_{confocal}$) (days 7 and 14 after treatment injection of liposomes). Right: Corresponding representative photomicrographs of CD31 and VEGFR2 staining. X20.

Fig. 9 Confocal microscopy of confocal ultrasound ($US_{confocal}$)-treated G-Dunning prostatic tumor 4 d after injection of liposomal doxorubicin (L-DXR) viz. 2 d after $US_{confocal}$ treatment. The signal of internalized doxorubicin (autofluorescence) is in red and perfused in green vessel (fluorescein isothiocyanate-lectin-conjugated staining). Top: Scan of the entire tumor section. Bar = 1000 µm. Bottom: Magnifications at the level of the periphery (left), transitional zone (center) and core of the tumor (right). Bar = 20 µm.

REFERENCES.

Abri Aghdam M, Bagheri R, Mosafer J, Baradaran B, Hashemzaei M, Baghbanzadeh A, de la Guardia M, Mokhtarzadeh A. Recent advances on thermosensitive and pH-sensitive liposomes employed in controlled release. Journal of controlled release : official journal of the Controlled Release Society 2019; 315:1-22.

Afadzi M, Strand SP, Nilssen EA, Masoy SE, Johansen TF, Hansen R, Angelsen BA, de LDC. Mechanisms of the ultrasound-mediated intracellular delivery of liposomes and dextrans. IEEE transactions on ultrasonics, ferroelectrics, and frequency control 2013; 60:21-33.

Aydin O, Chandran P, Lorsung RR, Cohen G, Burks SR, Frank JA. The Proteomic Effects of Pulsed Focused Ultrasound on Tumor Microenvironments of Murine Melanoma and Breast Cancer Models. Ultrasound in medicine & biology 2019; 45:3232-45.

Bachawal S, Bean GR, Krings G, Wilson KE. Evaluation of ductal carcinoma in situ grade via triple-modal molecular imaging of B7-H3 expression. npj Breast Cancer 2020; 6.

Bulbake U, Doppalapudi S, Kommineni N, Khan W. Liposomal Formulations in Clinical Use: An Updated Review. Pharmaceutics 2017; 9.

Camus M, Vienne A, Mestas JL, Pratico C, Nicco C, Chereau C, Marie JM, Moussatov A, Renault G, Batteux F, Lafon C, Prat F. Cavitation-induced release of liposomal chemotherapy in orthotopic murine pancreatic cancer models: A feasibility study. Clin Res Hepatol Gastroenterol 2019; 43:669-81.

Deshpande N, Pysz MA, Willmann JK. Molecular ultrasound assessment of tumor angiogenesis. Angiogenesis 2010; 13:175-88.

Dhaliwal A, Zheng G. Improving accessibility of EPR-insensitive tumor phenotypes using EPR-adaptive strategies: Designing a new perspective in nanomedicine delivery. Theranostics 2019; 9:8091-108.

Diakova GB, Du Z, Klibanov AL. Targeted Ultrasound Contrast Imaging of Tumor Vasculature With Positively Charged Microbubbles. Investigative radiology 2020; 55:736-40.

El Kaffas A, Hoogi A, Zhou J, Durot I, Wang H, Rosenberg J, Tseng A, Sagreiya H, Akhbardeh A, Rubin DL, Kamaya A, Hristov D, Willmann JK. Spatial Characterization of Tumor Perfusion Properties from 3D DCE-US Perfusion Maps are Early Predictors of Cancer Treatment Response. Sci Rep 2020; 10:6996.

El Kaffas A, Sigrist RMS, Fisher G, Bachawal S, Liau J, Wang H, Karanany A, Durot I, Rosenberg J, Hristov D, Willmann JK. Quantitative Three-Dimensional Dynamic Contrast-Enhanced Ultrasound Imaging: First-In-Human Pilot Study in Patients with Liver Metastases. Theranostics 2017; 7:3745-58.

Escoffre JM, Zeghimi A, Novell A, Bouakaz A. In-vivo gene delivery by sonoporation: recent progress and prospects. Curr Gene Ther 2013; 13:2-14.

Evjen TJ, Hupfeld S, Barnert S, Fossheim S, Schubert R, Brandl M. Physicochemical characterization of liposomes after ultrasound exposure - mechanisms of drug release. Journal of pharmaceutical and biomedical analysis 2013; 78-79:118-22.

Evjen TJ, Nilssen EA, Fowler RA, Rognvaldsson S, Brandl M, Fossheim SL. Lipid membrane composition influences drug release from dioleoylphosphatidylethanolamine-based liposomes on exposure to ultrasound. International journal of pharmaceutics 2011; 406:114-6.

615 Fant C, Lafond M, Rogez B, Castellanos IS, Ngo J, Mestas JL, Padilla F, Lafon C. In vitro
616 potentiation of doxorubicin by unseeded controlled non-inertial ultrasound cavitation.
617 Sci Rep 2019; 9:15581.
618 Fowler RA, Fossheim SL, Mestas JL, Ngo J, Canet-Soulas E, Lafon C. Non-invasive magnetic
619 resonance imaging follow-up of sono-sensitive liposome tumor delivery and controlled
620 release after high-intensity focused ultrasound. Ultrasound in medicine & biology
621 2013; 39:2342-50.
622 Frinking P, Segers T, Luan Y, Tranquart F. Three Decades of Ultrasound Contrast Agents: A
623 Review of the Past, Present and Future Improvements. Ultrasound in medicine &
624 biology 2020; 46:892-908.
625 Furusawa Y, Hassan MA, Zhao QL, Ogawa R, Tabuchi Y, Kondo T. Effects of therapeutic
626 ultrasound on the nucleus and genomic DNA. Ultrasonics sonochemistry 2014;
627 21:2061-8.
628 Golombek SK, May JN, Theek B, Appold L, Drude N, Kiessling F, Lammers T. Tumor targeting
629 via EPR: Strategies to enhance patient responses. Advanced drug delivery reviews
630 2018; 130:17-38.
631 Goncalves M, Mignani S, Rodrigues J, Tomas H. A glance over doxorubicin based-
632 nanotherapeutics: From proof-of-concept studies to solutions in the market. Journal
633 of controlled release : official journal of the Controlled Release Society 2019.
634 Gray MD, Lyon PC, Mannaris C, Folkes LK, Stratford M, Campo L, Chung DYF, Scott S, Anderson
635 M, Goldin R, Carlisle R, Wu F, Middleton MR, Gleeson FV, Coussios CC. Focused
636 Ultrasound Hyperthermia for Targeted Drug Release from Thermosensitive Liposomes:
637 Results from a Phase I Trial. Radiology 2019; 291:232-38.

638 Helbert A, Von Wronski M, Colevret D, Botteron C, Padilla F, Bettinger T, Tardy I, Hyvelin JM.
639 Ultrasound Molecular Imaging With BR55, a Predictive Tool of Antiangiogenic
640 Treatment Efficacy in a Chemo-Induced Mammary Tumor Model. Investigative
641 radiology 2020.
642 Horowitz AT, Barenholz Y, Gabizon AA. In vitro cytotoxicity of liposome-encapsulated
643 doxorubicin: dependence on liposome composition and drug release. Biochimica et
644 biophysica acta 1992; 1109:203-9.
645 Hyvelin JM, Tardy I, Arbogast C, Costa M, Emmel P, Helbert A, Theraulaz M, Nunn AD,
646 Tranquart F. Use of ultrasound contrast agent microbubbles in preclinical research:
647 recommendations for small animal imaging. Investigative radiology 2013; 48:570-83.
648 James JS. DOXIL approved for KS. AIDS treatment news 1995:6.
649 Kibria G, Hatakeyama H, Sato Y, Harashima H. Anti-tumor effect via passive anti-angiogenesis
650 of PEGylated liposomes encapsulating doxorubicin in drug resistant tumors.
651 International journal of pharmaceutics 2016; 509:178-87.
652 Klibanov AL. Ultrasound Contrast: Gas Microbubbles in the Vasculature. Investigative
653 radiology 2020.
654 Kondo T, Yoshii G. Effect of intensity of 1.2 MHz ultrasound on change in DNA synthesis of
655 irradiated mouse L cells. Ultrasound in medicine & biology 1985; 11:113-9.
656 Lafond M, Mestas JL, Prieur F, Chettab K, Geraci S, Clezardin P, Lafon C. Unseeded Inertial
657 Cavitation for Enhancing the Delivery of Chemotherapies: A Safety Study. Ultrasound
658 in medicine & biology 2016; 42:220-31.
659 Lee Y, Thompson DH. Stimuli-responsive liposomes for drug delivery. Wiley interdisciplinary
660 reviews. Nanomedicine and nanobiotechnology 2017; 9.

661 Leong-Poi H, Christiansen J, Klibanov AL, Kaul S, Lindner JR. Noninvasive Assessment of
662 Angiogenesis by Ultrasound and Microbubbles Targeted to α v -Integrins. Circulation
663 2003; 107:455-60.
664 Lyon PC, Gray MD, Mannaris C, Folkes LK, Stratford M, Campo L, Chung DYF, Scott S, Anderson
665 M, Goldin R, Carlisle R, Wu F, Middleton MR, Gleeson FV, Coussios CC. Safety and
666 feasibility of ultrasound-triggered targeted drug delivery of doxorubicin from
667 thermosensitive liposomes in liver tumours (TARDOX): a single-centre, open-label,
668 phase 1 trial. The lancet oncology 2018; 19:1027-39.
669 Matsumura Y, Maeda H. A New Concept for Macromolecular Therapeutics in Cancer
670 Chemotherapy: Mechanism of Tumoritropic Accumulation of Proteins and the
671 Antitumor Agent Smancs. Cancer research 1986; 46:6387-92.
672 Mestas JL, Fowler RA, Evjen TJ, Somaglino L, Moussatov A, Ngo J, Chesnais S, Rognvaldsson S,
673 Fossheim SL, Nilssen EA, Lafon C. Therapeutic efficacy of the combination of
674 doxorubicin-loaded liposomes with inertial cavitation generated by confocal
675 ultrasound in AT2 Dunning rat tumour model. Journal of drug targeting 2014.
676 Moghimi SM, Farhangrazi ZS. Just so stories: The random acts of anti-cancer nanomedicine
677 performance. Nanomedicine : nanotechnology, biology, and medicine 2014.
678 Nichols JW, Bae YH. EPR: Evidence and fallacy. Journal of controlled release : official journal of
679 the Controlled Release Society 2014.
680 Park J, Choi Y, Chang H, Um W, Ryu JH, Kwon IC. Alliance with EPR Effect: Combined Strategies
681 to Improve the EPR Effect in the Tumor Microenvironment. Theranostics 2019; 9:8073-
682 90.

683 Payen T, Dizeux A, Baldini C, Le Guillou-Buffello D, Lamuraglia M, Comperat E, Lucidarme O,
684 Bridal SL. VEGFR2-Targeted Contrast-Enhanced Ultrasound to Distinguish between
685 Two Anti-Angiogenic Treatments. Ultrasound in medicine & biology 2015; 41:2202-11.
686 Pochon S, Tardy I, Bussat P, Bettinger T, Brochot J, von Wronski M, Passantino L, Schneider M.
687 BR55: a lipopeptide-based VEGFR2-targeted ultrasound contrast agent for molecular
688 imaging of angiogenesis. Investigative radiology 2010; 45:89-95.
689 Shim CY, Liu YN, Atkinson T, Xie A, Foster T, Davidson BP, Treible M, Qi Y, Lopez JA, Munday A,
690 Ruggeri Z, Lindner JR. Molecular Imaging of Platelet-Endothelial Interactions and
691 Endothelial von Willebrand Factor in Early and Mid-Stage Atherosclerosis. Circ
692 Cardiovasc Imaging 2015; 8:e002765.
693 Smeenge M, Tranquart F, Mannaerts CK, de Reijke TM, van de Vijver MJ, Laguna MP, Pochon
694 S, de la Rosette J, Wijkstra H. First-in-Human Ultrasound Molecular Imaging With a
695 VEGFR2-Specific Ultrasound Molecular Contrast Agent (BR55) in Prostate Cancer: A
696 Safety and Feasibility Pilot Study. Investigative radiology 2017; 52:419-27.
697 Somaglino L, Bouchoux G, Mestas JL, Lafon C. Validation of an acoustic cavitation dose with
698 hydroxyl radical production generated by inertial cavitation in pulsed mode:
699 application to in vitro drug release from liposomes. Ultrasonics sonochemistry 2011;
700 18:577-88.
701 Sridharan A, Eisenbrey JR, Machado P, Ojeda-Fournier H, Wilkes A, Sevrukov A, Mattrey RF,
702 Wallace K, Chalek CL, Thomenius KE, Forsberg F. Quantitative analysis of vascular
703 heterogeneity in breast lesions using contrast-enhanced 3-D harmonic and
704 subharmonic ultrasound imaging. IEEE transactions on ultrasonics, ferroelectrics, and
705 frequency control 2015; 62:502-10.

Swetha KL, Roy A. Tumor heterogeneity and nanoparticle-mediated tumor targeting: the importance of delivery system personalization. Drug Deliv Transl Res 2018; 8:1508-26.

Tardy I, Pochon S, Theraulaz M, Emmel P, Passantino L, Tranquart F, Schneider M. Ultrasound molecular imaging of VEGFR2 in a rat prostate tumor model using BR55. Investigative radiology 2010; 45:573-8.

Thorn CF, Oshiro C, Marsh S, Hernandez-Boussard T, McLeod H, Klein TE, Altman RB. Doxorubicin pathways: pharmacodynamics and adverse effects. Pharmacogenetics and genomics 2011; 21:440-6.

Tranquart F, Mercier L, Frinking P, Gaud E, Arditi M. Perfusion quantification in contrast-enhanced ultrasound (CEUS)--ready for research projects and routine clinical use. Ultraschall Med 2012; 33 Suppl 1:S31-8.

Villemain O, Robin J, Bel A, Kwiecinski W, Bruneval P, Arnal B, Rémond M, Tanter M, Messas E, Pernot M. Pulsed Cavitational Ultrasound Softening: a new non-invasive therapeutic approach of calcified bioprosthetic valve stenosis. JACC Basic Transl Sci 2017; 2:372-83.

Wang S, Hossack JA, Klibanov AL. From Anatomy to Functional and Molecular Biomarker Imaging and Therapy. Investigative radiology 2020; Publish Ahead of Print.

Willmann JK, Bonomo L, Testa AC, Rinaldi P, Rindi G, Valluru KS, Petrone G, Martini M, Lutz AM, Gambhir SS. Ultrasound Molecular Imaging With BR55 in Patients With Breast and Ovarian Lesions: First-in-Human Results. Journal of clinical oncology : official journal of the American Society of Clinical Oncology 2017; 35:2133-40.

Wischhusen J, Wilson KE, Delcros JG, Molina-Pena R, Gibert B, Jiang S, Ngo J, Goldschneider D, Mehlen P, Willmann JK, Padilla F. Ultrasound molecular imaging as a non-invasive

729 companion diagnostic for netrin-1 interference therapy in breast cancer. Theranostics
730 2018; 8:5126-42.
731 Xiang H, Huang R, Cheng J, Gulinaer S, Hu R, Feng Y, Liu H. Value of three-dimensional contrast-
732 enhanced ultrasound in the diagnosis of small adnexal masses. Ultrasound in medicine
733 & biology 2013; 39:761-8.
734 Zhao F, Unnikrishnan S, Herbst EB, Klibanov AL, William Mauldin F, Jr., Hossack JA. A Targeted
735 Molecular Localization Imaging Method Applied to Tumor Microvasculature. Investigative radiology 2020.
736
737 Zhou Q, Dong C, Fan W, Jiang H, Xiang J, Qiu N, Piao Y, Xie T, Luo Y, Li Z, Liu F, Shen Y. Tumor
738 extravasation and infiltration as barriers of nanomedicine for high efficacy: The current
739 status and transcytosis strategy. Biomaterials 2020; 240:119902.
740

a **Pharmacokinetic and biodistribution of doxorubicin (F-DXR) and Liposomal doxorubicin (L-DXR) in blood, tumor and surrounding tissue**

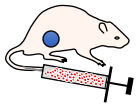

t0	t24h	t48h	t72h
Injection:	Blood, tissue sampling:	Blood, tissue sampling:	Blood, tissue sampling:
F-DXR (n = 7) L-DXR (n = 9)	F-DXR (n = 2) L-DXR (n = 2)	F-DXR (n = 3) L-DXR (n = 3)	F-DXR (n = 2) L-DXR (n = 4)

b **Evaluation of the $US_{confocal}$ treatment on histopathology and L-DXR +/- $US_{confocal}$ treatment on G-Dunning tumor growth assessed in B-mode over 7 days**

Histopathological evaluation of tumors 20 min after $US_{confocal}$ treatment
$US_{confocal}$ treated tumor (n=5), Control tumor (n=1).

Growth rate of tumor over 7-days
$US_{confocal}$ treated tumor (n=5), Control tumor(n=4), L-DXR (n=9), L-DXR + $US_{confocal}$ (n=7).

c **Evaluation of L-DXR vs. L-DXR + $US_{confocal}$ on G-Dunning tumors by USMI/B-mode and IHC**

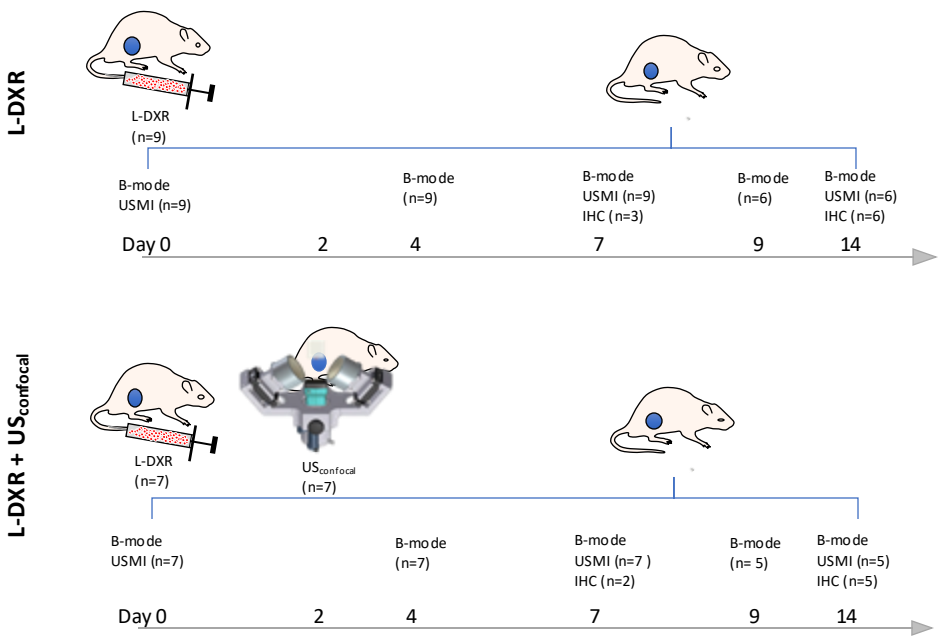

Figure 1

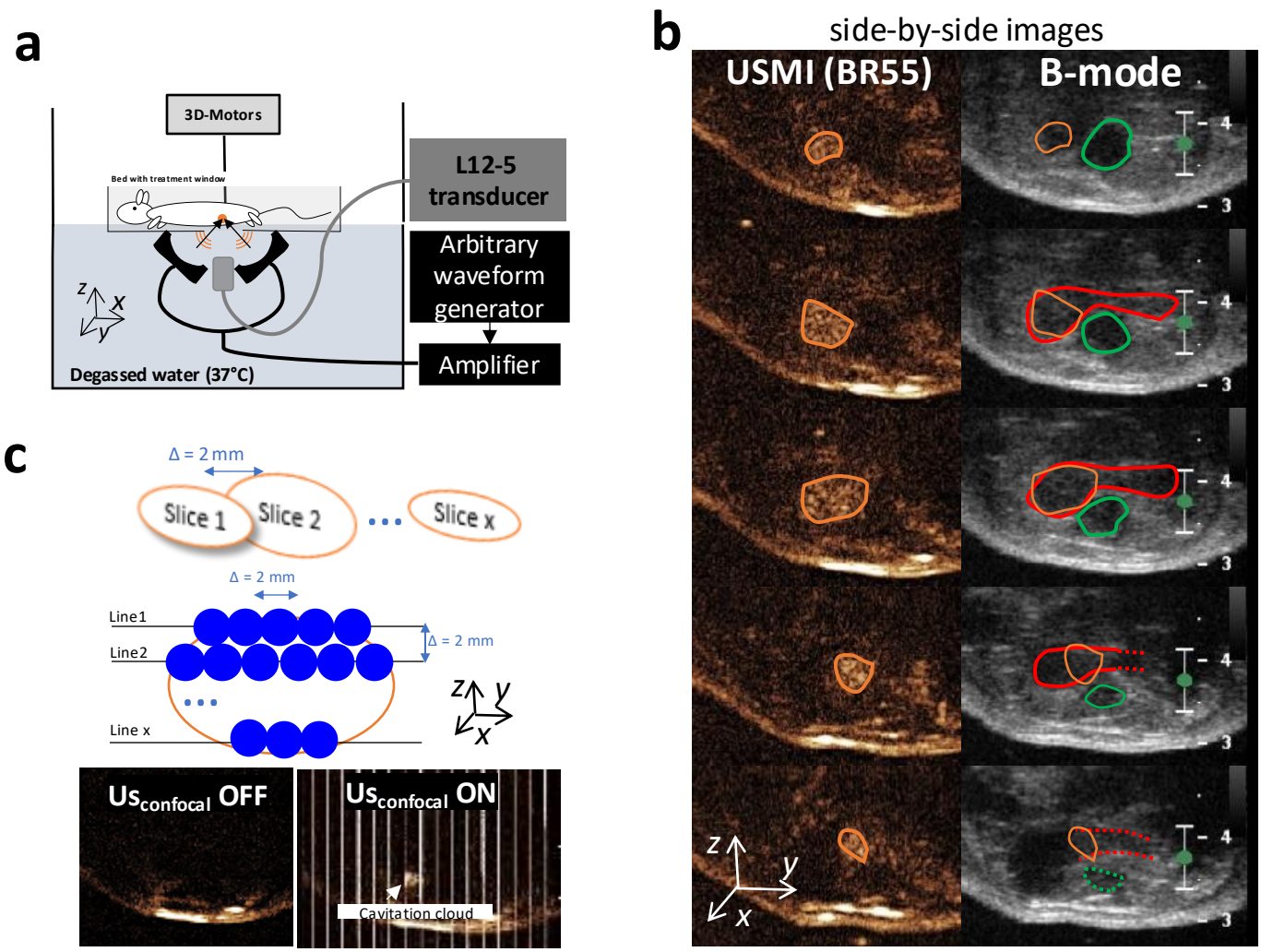
a
3D-Motors
Bed with treatment window
L12-5 transducer
Arbitrary waveform generator
Amplifier
Degassed water (37°C)
z
x
y
b
side-by-side images
USMI (BR55)
B-mode
c
Δ = 2 mm
Slice 1
Slice 2
Slice x
Δ = 2 mm
Line1
Line2
Line x
Δ = 2 mm
Us confocal OFF
Us confocal ON
Cavitation cloud

Figure 2

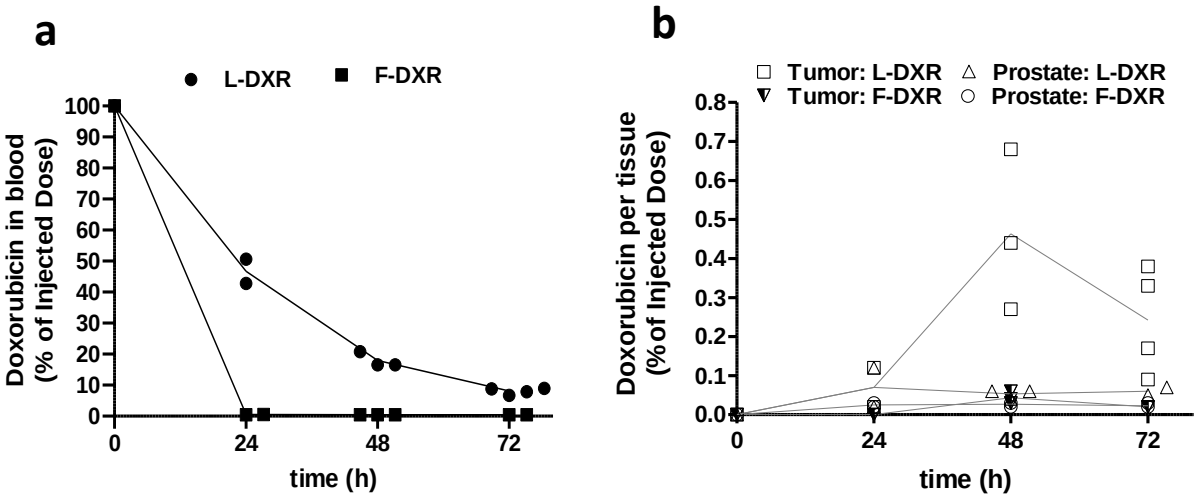
a
L-DXR
F-DXR
Doxorubicin in blood
(% of Injected Dose)
100
90
80
70
60
50
40
30
20
10
0
0
24
48
72
time (h)
b
Tumor: L-DXR
Prostate: L-DXR
Tumor: F-DXR
Prostate: F-DXR
Doxorubicin per tissue
(% of Injected Dose)
0.8
0.7
0.6
0.5
0.4
0.3
0.2
0.1
0.0
0
24
48
72
time (h)

Figure 3

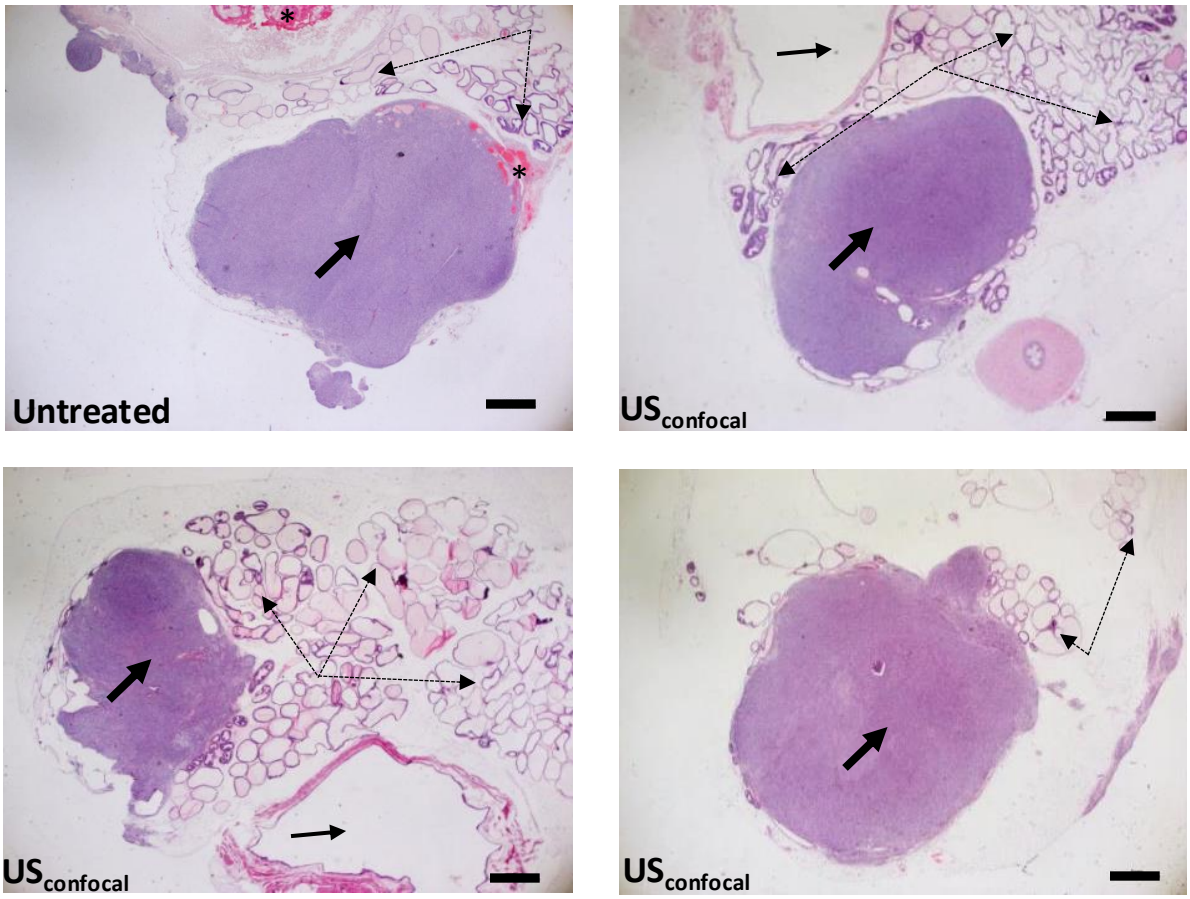

Figure 4

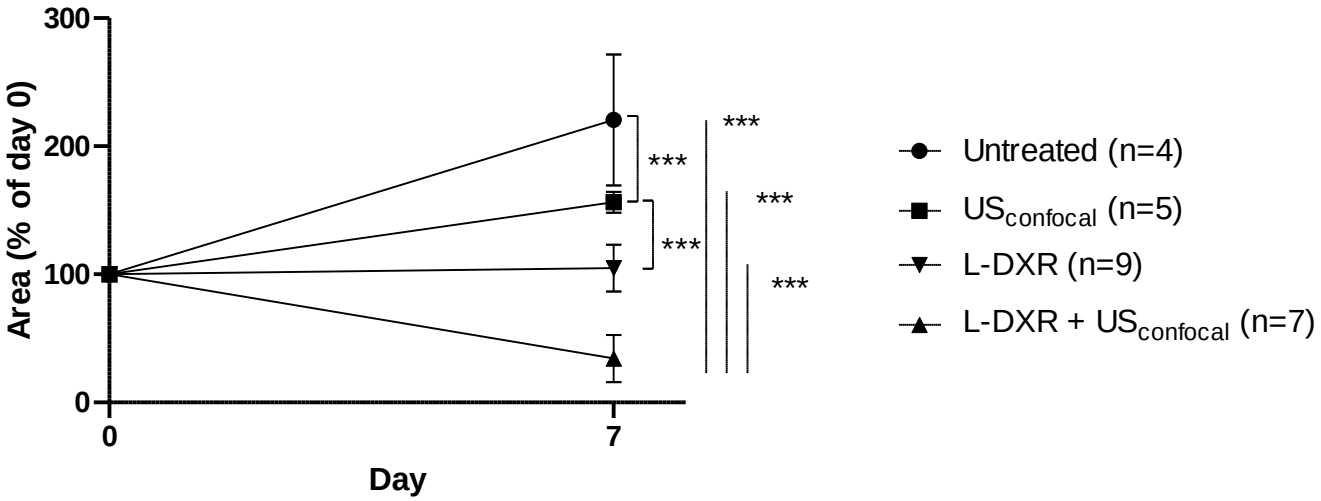
300
200
100
0
Area (% of day 0)
0
7
Day
***
***
***
***
Untreated (n=4)
US confocal (n=5)
L-DXR (n=9)
L-DXR + US confocal (n=7)

Figure 5

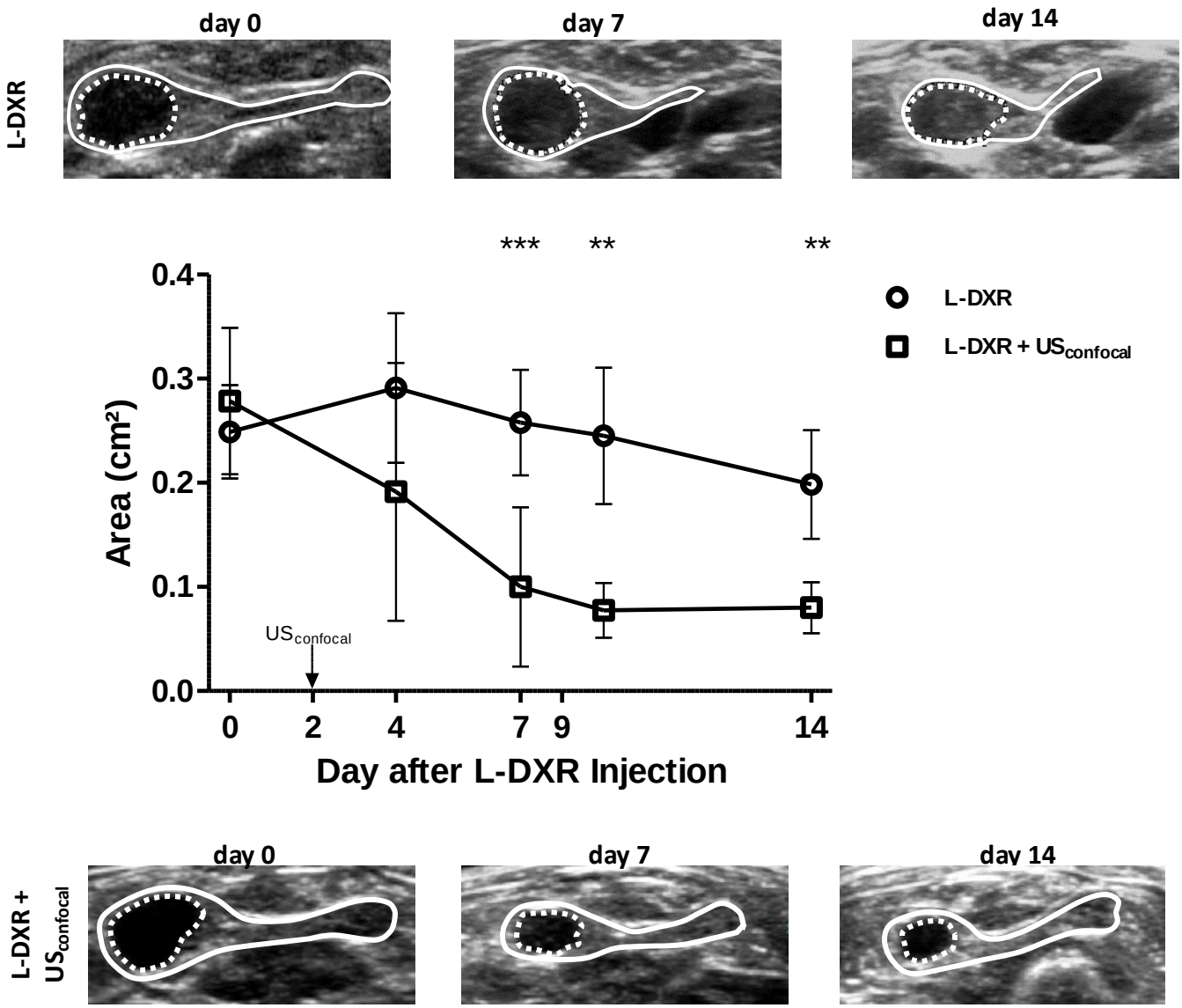
day 0
day 7
day 14
L-DXR
***
**
**
0.4
0.3
0.2
0.1
0.0
Area (cm²)
US confocal
0
2
4
7
9
14
Day after L-DXR Injection
L-DXR
L-DXR + US confocal
day 0
day 7
day 14
L-DXR + US confocal

Figure 6

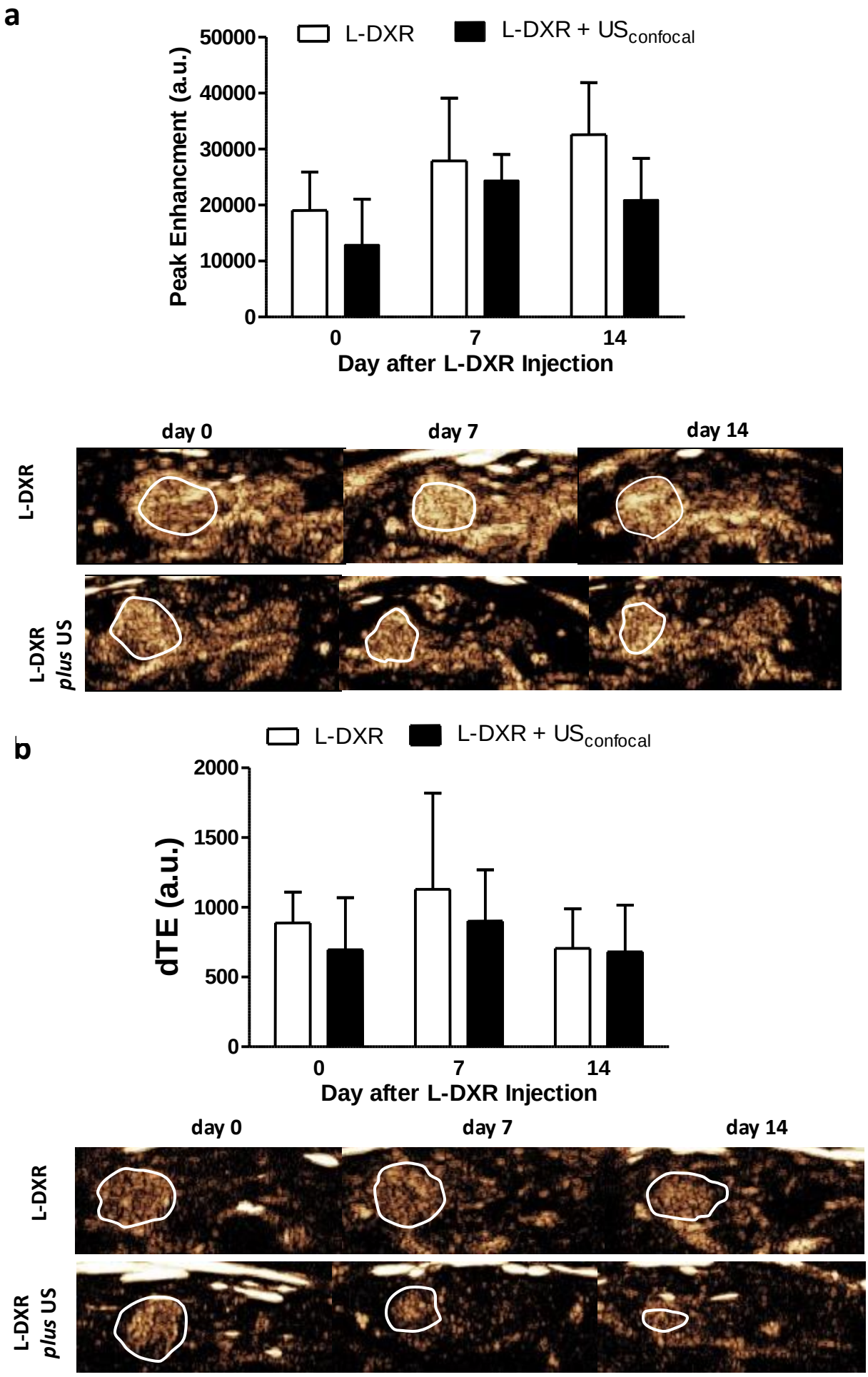
a
L-DXR
L-DXR + US confocal
Peak Enhancment (a.u.)
50000
40000
30000
20000
10000
0
0
7
14
Day after L-DXR Injection
day 0
day 7
day 14
L-DXR
L-DXR plus US
b
L-DXR
L-DXR + US confocal
dTE (a.u.)
2000
1500
1000
500
0
0
7
14
Day after L-DXR Injection
day 0
day 7
day 14
L-DXR
L-DXR plus US

Figure 7

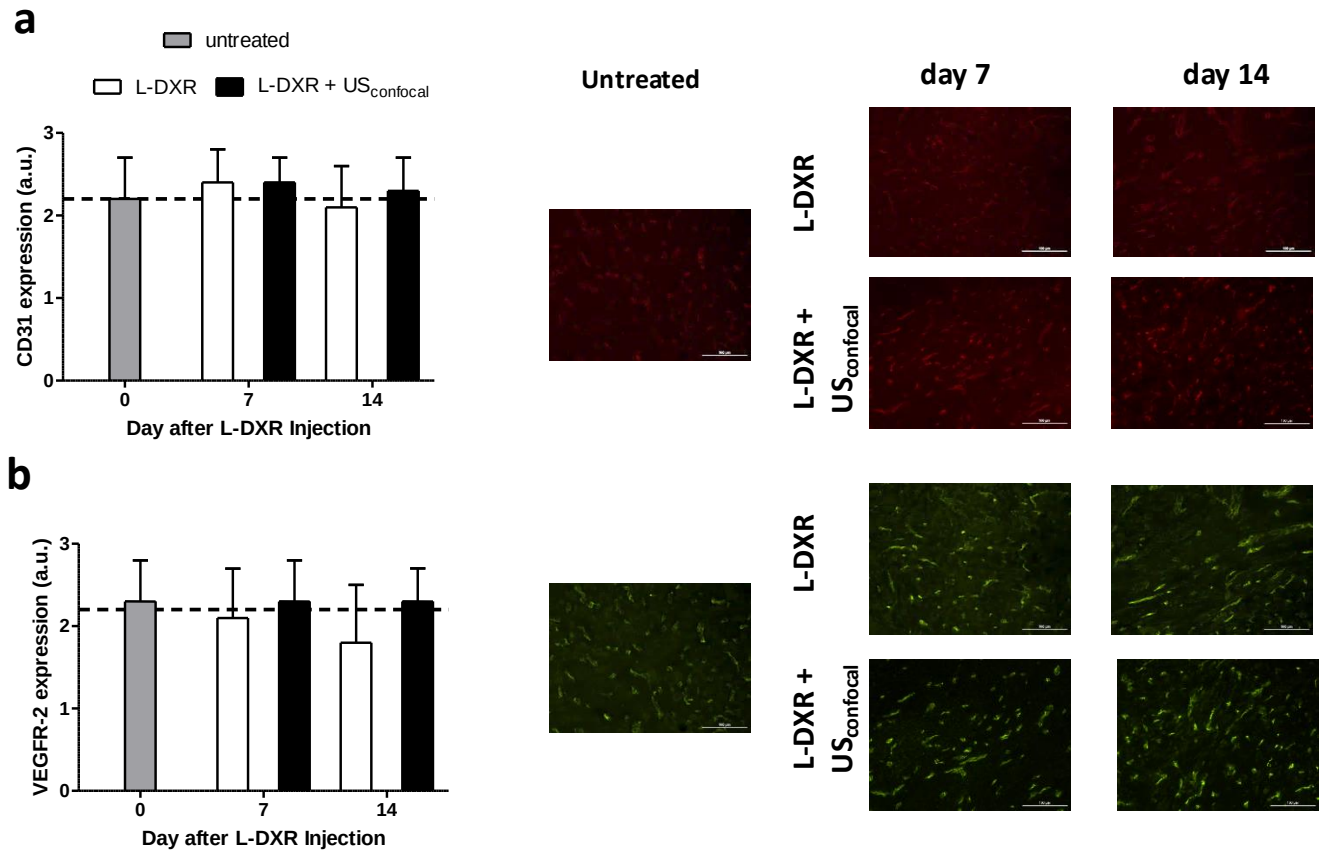
a
untreated
L-DXR
L-DXR + US confocal
CD31 expression (a.u.)
0
1
2
3
0
7
14
Day after L-DXR Injection
Untreated
day 7
day 14
L-DXR
L-DXR + US confocal
b
VEGFR-2 expression (a.u.)
0
1
2
3
0
7
14
Day after L-DXR Injection
L-DXR
L-DXR + US confocal

Figure 8

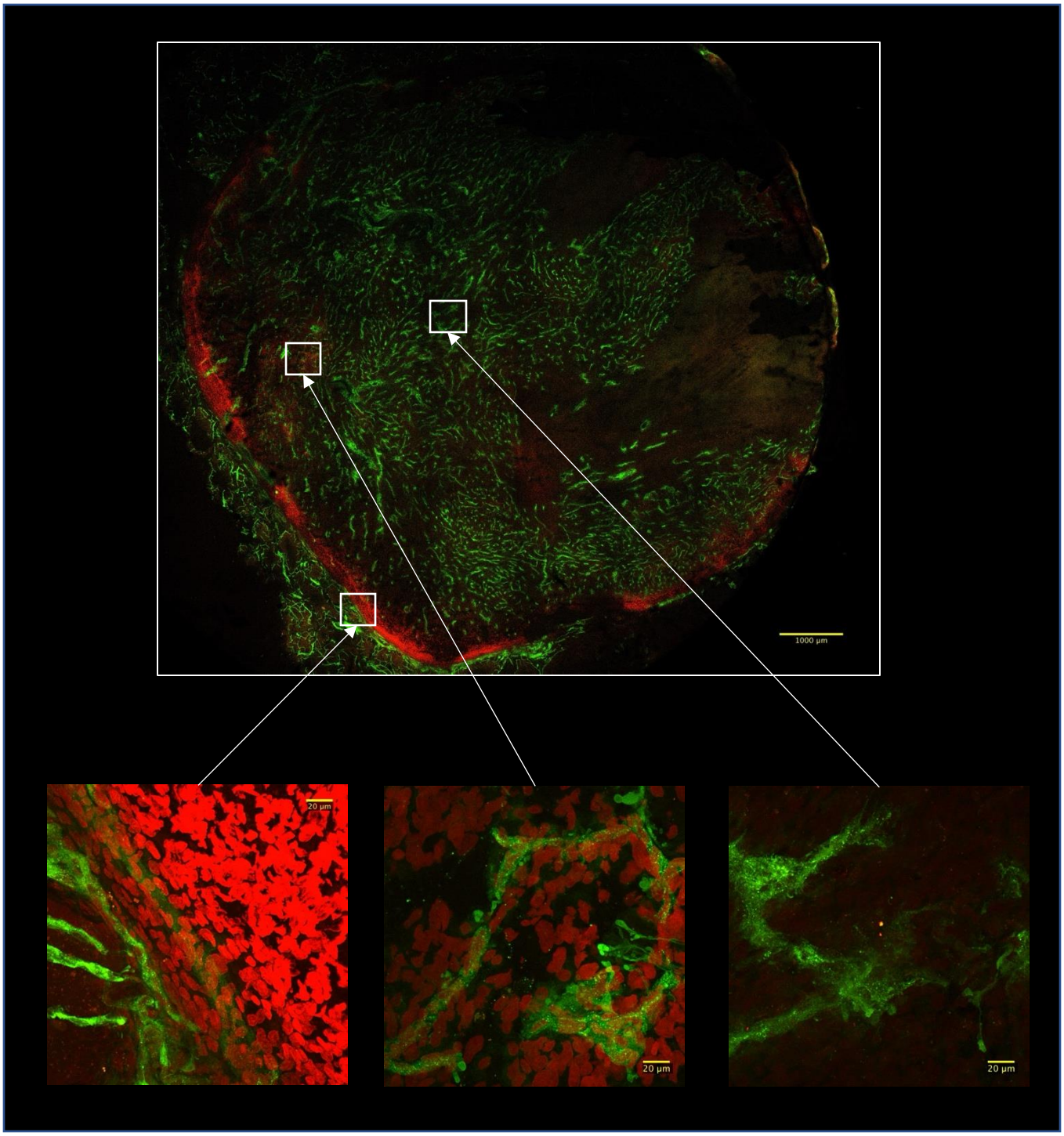

Figure 9